ADVANCED MATERIALS
www.advmat.de
www.MaterialsViews.com

COMMUNICATION

Core–Shell Pd@Au Nanoplates as Theranostic Agents for In-Vivo Photoacoustic Imaging, CT Imaging, and Photothermal Therapy

Mei Chen, Shaoheng Tang, Zhide Guo, Xiaoyong Wang, Shiguang Mo, Xiaoqing Huang, Gang Liu, and Nanfeng Zheng**

Two-dimensional (2D) nanomaterials with a nanoscale thickness have recently attracted much attention owing to their unique physical and chemical properties induced by the quantum size and surface effects.[1] For instance, graphene as a typical 2D nanostructure, with ultra-high specific surface area and strong near-infrared (NIR) optical absorbance, has been widely applied in biomedicine and other related fields.[2] Inspired by graphene, more and more attention has been directed to bioapplications (e.g., photothermal therapy, imaging) of many other inorganic 2D nanostructures that exhibit excellent optical properties and biocompatibility. By intratumoral injection, Bi_2Se_3 nanoplates were successfully applied in photothermal ablation of tumors.[3] Transition-metal dichalcogenides with 2D nanostructures, such as MoS_2 and WS_2 nanosheets, were also demonstrated as effective photothermal cancer therapy agents in vitro and in vivo.[4] Despite the intense interest, considerable challenges remain in the development of desirable 2D nanostructures for NIR photothermal therapy. In particular, few nanomaterials with well-defined thickness and diameters have been obtained using the synthetic methods developed so far.[1a,4a,5]

As for photothermal cancer therapy, quite several classes of nanomaterials (e.g., Au nanorods,[6] nanoshells,[7] nanocages,[8] nanostars[9] that display strong absorbance and significant photothermal effect in the NIR region have been widely explored in the past decade. However, to make them highly effective for therapeutic purpose, photothermal therapeutic agents need to be specifically targeted to tumor sites, which can minimize not only the laser power density but also the amount of therapeutic agents. In the literature, effective photothermal ablation of cancer cells in vitro was readily achieved by photothermal agents conjugated with targeting ligands.[10] Due to the high uptake in RES (reticuloendothelial) system and fast clearance from blood, it still however remains a great challenge to enhance in vivo photothermal therapeutic effects of nanomaterials.[9–11] To tackle this challenge, surface modification of polyethylene glycol (PEG) was typically introduced to achieve prolonged blood circulation time and lower in vivo toxicity.[12] For example, PEGylated graphene nanosheets exhibited very highly efficient tumor passive targeting and relatively low retention in RES systems.[2b] It was also reported that the geometry of nanomaterials played an important role in their accumulation behaviors on tumor sites.[13] Graphene nanosheets were demonstrated to have higher accumulation in tumor tissues than carbon nanotubes. Besides carbon nanomaterials, however, more studies are still needed to illustrate the advantages of 2D nanostructures for targeting tumors.

Recently, we have successfully synthesized ultrathin freestanding hexagonal palladium nanosheets with well-defined thicknesses, sizes, and tunable surface plasmon resonance (SPR) peak in the NIR region.[14] Moreover, other noble metals were readily epitaxially grown on the surface of Pd nanosheets,[15] providing us with great opportunities to synthesize well-defined noble metal nanoplates and study their in vivo behaviors. With these developments, we report herein a novel image-guided photothermal cancer therapy platform based on core–shell Pd@Au nanoplates. The core–shell Pd@Au nanoplates were synthesized by a seeded growth method using Pd nanosheets, with well-defined shapes and sizes, as seeds. The synthesized core–shell Pd@Au nanoplates showed strong NIR absorbance and excellent stability. By modifying their surface with thiol-polyethylene glycol (SH-PEG), the blood circulation of PEGylated Pd@Au nanoplates (Pd@Au-PEG) in vivo was prolonged. Through passive targeting, the accumulation of Pd@Au-PEG in tumor site was higher than spherical Au nanoparticles with a similar hydrodynamic size. Using Pd@Au-PEG as the NIR photothermal agent, photothermal ablation of tumors was achieved under the irradiation of 808 nm laser at a power density of only 0.5 W cm^{-2}. Their applications of the Pd@Au-PEG as photoacoustic (PA) and computed tomography (CT) contrast agent were demonstrated as well.

In a typical synthesis of Pd@Au core–shell nanoplates, hexagonal Pd nanosheets with an average edge length of

M. Chen, Dr. S. H. Tang, S. G. Mo, Dr. X. Q. Huang, Prof. N. F. Zheng
State Key Laboratory for Physical Chemistry of Solid Surfaces, Collaborative Innovation Center of Chemistry for Energy Materials and Department of Chemistry
College of Chemistry and Chemical Engineering
Xiamen University
Xiamen 361005, P.R. China
E-mail: nfzheng@xmu.edu.cn
Z. D. Guo, Dr. X. Y. Wang, Prof. G. Liu
State Key Laboratory of Molecular Vaccinology and Molecular Diagnostics
Center for Molecular Imaging and Translational Medicine
School of Public Health
Xiamen University
Xiamen 361005, P.R. China
E-mail: gangliu.cmitm@xmu.edu.cn

DOI: 10.1002/adma.201404013

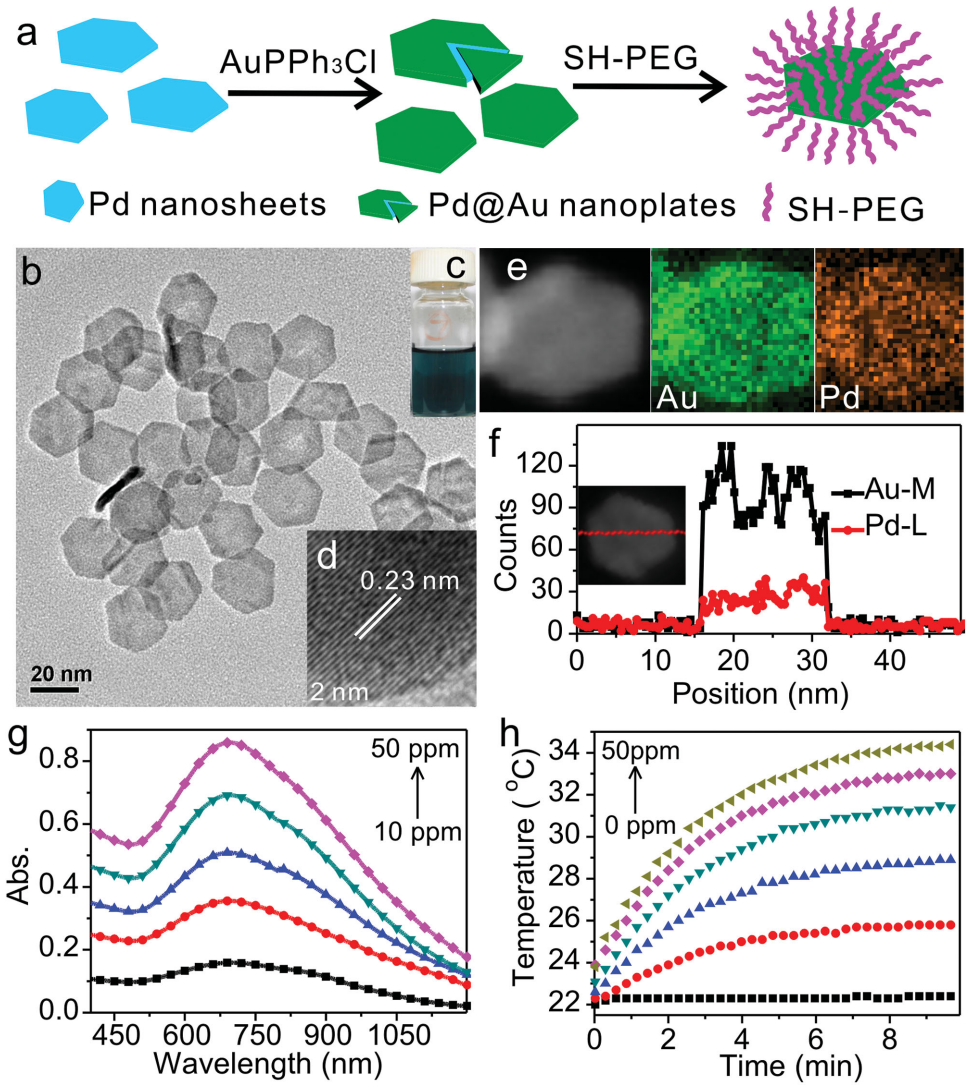

Figure 1. Synthesis and characterizations of Pd@Au nanoplates. a) Scheme shows the fabrication process of Pd@Au nanoplates. b) Representative TEM image. c) Photograph of a water dispersion of the as-prepared Pd@Au nanoplates. d) HRTEM image of a Pd@Au nanoplate flat lying on the TEM grid. e) HAADF-STEM image and EDX mapping images of a Pd@Au nanoplate. f) EDX line profiles of the Pd@Au nanoplate as shown in the left inset HAADF-STEM image. g) UV-Vis-NIR absorption of Pd@Au nanoplates with different concentrations. h) Temperature rise curves of Pd@Au nanoplates with different concentrations upon 0.5 W cm^{-2} 808 nm laser irradiation.

≈15 nm and a thickness of 1.8 nm were first synthesized (see the Experimental Section for details; Figure S1, Supporting Information) and used as seeds for the formation of bimetallic Pd@Au nanoplates (**Figure 1**a). The overgrowth of Au on Pd nanosheets was achieved by chemically reducing $AuPPh_3Cl$ with hydrazine hydrate in *N,N*-dimethylformamide, with a Au/Pd mole ratio of 10:1. The obtained Pd@Au nanoplates exhibited a deep aquamarine color in aqueous solution (Figure 1c). As shown in the representative transmission electron microscopy (TEM) image of the as-made core–shell Pd@Au nanoplates (Figure 1b), the nanoplates still adopted a hexagonal plate-like shape and had a mean diameter of ≈30 nm, similar to that of Pd nanosheet seeds. However, the average thickness of the Pd@Au nanosheets was ≈4 nm, larger than that of Pd nanosheets. As illustrated in the high-resolution TEM (HRTEM) image (Figure 1d), the core–shell Pd@Au nanoplates were highly crystalline. Well-defined lattice fringes with d-spacing of 2.3 Å corresponding to the {111} planes of Au were clearly observed. Moreover, the elemental distribution of Au on Pd nanosheets was studied by energy-dispersive X-ray (EDX) spectroscopy. Both the elemental-mapping analysis (Figure 1e) and the EDX line profile (Figure 1f) revealed that both Au and Pd atoms were homogeneously distributed throughout the as-prepared core–shell Pd@Au nanoplates, suggesting that Au was successfully epitaxially overgrown on the Pd nanosheets.

As previously reported,[14–16] the SPR properties of 2D metal nanostructures are tunable depending on their diameter and thickness. Herein, by changing the sizes of Pd nanosheet seeds, different-sized Pd@Au nanoplates with SPR peaks ranging from 600 nm to 1300 nm (Figure S1, Supporting Information) were readily prepared. As shown in Figure 1f, with an average diameter of 30 nm and thickness of 4 nm, the as-prepared Pd@

Au nanosheets dispersed in water exhibited a strong absorption with a peak centered at 700 nm but extended into the NIR region. To demonstrate the potential of Pd@Au nanoplates as an NIR photothermal therapy agent, the photothermal effect of Pd@Au nanoplates was investigated by monitoring the temperature increase of 1 mL aqueous solution containing Pd@Au nanoplates at different concentrations upon NIR irradiation. Under a given laser power, the temperature increase is determined by the concentration of the photothermal agent and the irradiation time as well. Experimentally, we examined the temperature changes during the course of 10 min irradiation by the 808 nm laser with a power density of 0.5 W cm^{-2}. As shown in Figure 1g, while the control experiment using pure water gave a temperature increase of less than 2 °C, the temperature of the solution containing 50 ppm Pd@Au was increased by up to 15 °C in 10 min irradiation. According to the previous reported method,[17] the photothermal conversion efficiency of Pd@Au-PEG was calculated to be 28.6%, which is comparable to that of gold nanorods (22%) and gold nanoshells (13%). Moreover, Pd@Au-PEG exhibited excellent stability in different media at 37 °C, and the absorbance at 808 nm did not change under laser irradiation (808 nm, 0.5 W cm^{-2}) for 30 min (Figures S2 and S3, Supporting Information).

As measured by dynamic light scattering (DLS), the Pd@Au-PEG in aqueous solution showed a hydrodynamic size of ≈60 nm (Figure S4a, Supporting Information), larger than the size measured by TEM. The measurement of zeta potential indicated that the Pd@Au-PEG was nearly neutrally charged (Figure S4b, Supporting Information). It has been well documented that the surface modification by long-chained PEG molecules helps nanoparticles to escape from macrophage clearance in reticuloendothelial systems (RES) and thus prolong their circulation time in the blood. Consequently, their passive targeting to tumor sites can be enhanced.[18] The blood circulation of Pd@Au-PEG was thus studied to probe their in vivo behaviors. Experimentally, Balb/c mice were intravenously injected with Pd@Au-PEG at a dose of 15 mg kg^{-1} (300 µL of 1 mg mL^{-1} solution). Tail blood was drawn at different times and digested to measure the amount of Au in blood by inductively coupled plasma mass spectrometry (ICP-MS). As shown in **Figure 2**a, the blood circulation half-life time was as long as 8 h, allowing them to be passively targeted more to tumor sites.

To further study the in vivo biodistribution of Pd@Au-PEG, Balb/c mice bearing 4T1 murine breast cancer tumors were intravenously injected with Pd@Au-PEG at a dose of 15 mg kg^{-1} (300 µL, 1 mg mL^{-1}). The mice were then sacrificed at 1, 12, and 24 h after injection. Major organs and tissues (i.e., liver, tumor, heart, kidney, lung, spleen, skin, brain, stomach, and bone) were weighted and digested to determine the amounts of Au using ICP-MS. Surprisingly, as shown in Figure 2b, the highest accumulation of Pd@Au-PEG was revealed in tumors. The accumulations of Au in tumor sites were measured to be ≈2% ID g^{-1}, ≈15% ID g^{-1}, and ≈79% ID g^{-1} as the postinjection time was increased from 1 h, 12 h to 24 h. In comparison, the accumulations of Pd@Au-PEG in the liver and spleen were relatively low. After 24 h, the accumulations in the liver and spleen were ≈17% ID g^{-1} and ≈33% ID g^{-1}, respectively. The high accumulation of Pd@Au-PEG in tumor sites was attributed to the enhanced permeability and retention (EPR) effect due to

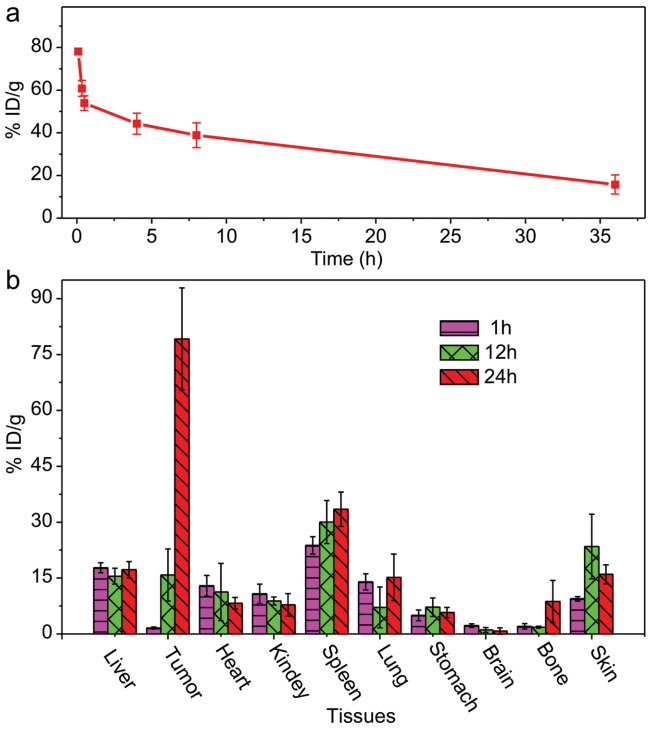

Figure 2. In vivo experiments of Pd@Au-PEG. a) Blood circulation curve of Pd@Au-PEG as determined by measuring the Au amount in blood at different time. b) Biodistribution of Pd@Au-PEG in different organs at 1, 12, and 24 h p.i. Error bars were based on 3–5 mice per point.

the tortuous and leaky nature of tumor vasculature. Besides the surface PEGylation, the unique 2D structural feature of Pd@Au nanoplates was critical to enhance their passive accumulation in tumors. For comparison, spherical Au nanoparticles with a similar size to that of Pd@Au-PEG were synthesized.[19] The accumulation of PEGylated spherical Au nanoparticles in tumor sites was measured to be only ≈19% ID g^{-1} at 24 h, much less than that of Pd@Au-PEG (Figure S5, Supporting Information). This result clearly demonstrated the importance of 2D morphology of Pd@Au nanoplates in enhancing their biodistribution for imaging and therapeutic purposes.

PA imaging is a newly developed and hybrid biomedical imaging modality that measures the ultrasonic waves induced by tissues' absorption (e.g., hemoglobin and melanin) of pulsed laser.[20] However, many diseases do not manifest an endogenous PA contrast due to their weak optical absorption. It is thus essential to develop exogenous PA contrast agents with excellent photothermal effect to convert NIR light into heat for acoustic imaging.[21] To demonstrate the PA imaging properties of Pd@Au-PEG, in vitro PA imaging was performed in vials using a PA instrument at the wavelengths of 700 nm. As shown in Figure S6 (Supporting Information), Pd@Au-PEG exhibited significant PA contrast effect, which motivated us to use PA imaging to visualize the in vivo accumulation behavior of Pd@Au-PEG with high spatial resolution and anatomical localization. Without the need to sacrifice mice, in this work, the PA imaging method allowed us to verify the high accumulation of Pd@Au-PEG in tumor sites as monitored by ICP-MS measurements. Experimentally, PA images of tumors with no

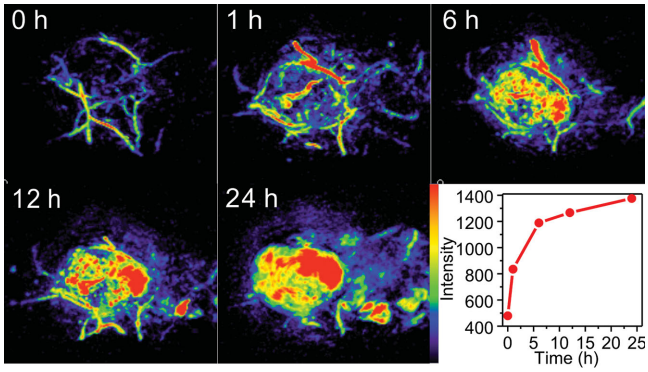

Figure 3. Photoacoustic imaging of Pd@Au-PEG in tumor sites and quantification photoacoustic signals of tumor site at different time.

treatment were firstly recorded. Pd@Au-PEG was then intravenously injected at a dose of 15 mg kg^{-1} (300 µL, 1 mg mL^{-1}). PA images were recorded at 1, 6, 12, and 24 h postinjection. As shown in **Figure 3**, only major blood vessels could be observed without Pd@Au-PEG. After the injection, the values of PA signals in tumor sites increased and the outline of tumor became much clear as time went on, indicating the gradual accumulation of Pd@Au-PEG in the tumor. The PA signals were more than four times enhanced after 24 h injected with Pd@Au-PEG. It should be pointed out that the accumulation behavior of Pd@Au-PEG observed by the in vivo PA imaging was consistent to that measured by ICP-MS.

X-ray CT is one of the most useful diagnostic tools in hospitals in terms of frequency of use and cost.[22] The use of Au nanoparticles as CT contrast agents has received considerable attention for their high X-ray absorption, good biocompatibility, and easy surface modification.[23] To assess the potential of Pd@Au-PEG as an effective CT contrast agent, the X-ray attenuation of Pd@Au-PEG with different concentrations was evaluated. As shown in **Figure 4**a,b, the CT signal intensity indeed increased with the concentration of Au. CT values and Pd@Au-PEG concentration displayed a well-correlated linear relationship. The good CT imaging performance of Pd@Au-PEG in vitro motivated us to further use Pd@Au-PEG for in vivo CT imaging. As shown in Figure 4c, the tumor CT images were obtained before and 24 h after intravenously injection of Pd@Au-PEG. The tumor site showed an obvious enhancement with a significantly higher CT value 24 h postinjection as shown in Figure 4d, which is again an evidence for the high accumulation in tumor sites.

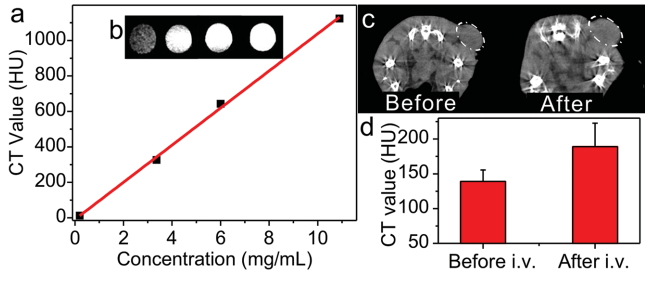

Figure 4. a) In vitro CT attenuation (HU) plot and b) CT images of Pd@Au-PEG with different concentrations. c) In vivo cross-sectional CT images and d) CT values of mice before and after Pd@Au-PEG.

Based on the above two types of imaging techniques, an image-guided photothermal therapy was carried out to investigate its cancer therapy application in vivo using 4T1 tumor model on Balb/c mice. Ten mice bearing 4T1 tumor at their right shoulder were intravenously injected with 300 µL of Pd@Au-PEG at 1 mg mL^{-1} (a dose of 15 mg kg^{-1}). Another 10 mice without Pd@Au-PEG injection were used as the control. As discussed above, the accumulation of Pd@Au-PEG in tumor sites was relatively high at 24 h postinjection. It is worth mentioning that the color of tumors on the mice injected with Pd@Au-PEG turned black at 24 h postinjection (**Figure 5**d). Interestingly, Pd@Au nanoplates could be observed by TEM measurements on the ultrathin section tumor samples (Figure S7, Supporting Information). Based on these results, we therefore treated the tumors with 808 nm laser at a power density of 0.5 W cm^{-2} at 24 h postinjection. As illustrated in Figure 5a and Figure S8 (Supporting Information), the surface temperature of tumors on Pd@Au-PEG-injected mice reached ≈60 °C only after 4 min laser irradiation. In comparison, less than 3 °C of surface temperature increase was observed for irradiated tumors on uninjected mice. Another two control groups of mice with and without Pd@Au-PEG injection were not irradiated. Tumor sizes were measured every other day after treatment. As shown in Figure 5b–d, all irradiated tumors on mice injected with Pd@Au-PEG disappeared after laser irradiation and no tumor regrowth was noted in this treated group over a course of 60 d. In marked contrast, tumors in the control untreated group, the irradiation only group (no Pd@Au-PEG injection), and the Pd@Au-PEG only group (no laser irradiation) showed relatively rapid tumor growth, demonstrating that the NIR laser irradiation or Pd@Au-PEG injection by itself did not affect the tumor development. Mice in these three control groups showed average life spans of no more than ≈20 d, while mice in the treated group were tumor-free after treatment (Pd@Au-PEG injection, NIR laser irradiation) and survived over 60 d without a single death, further demonstrating the excellent efficacy of Pd@Au-PEG-based in vivo photothermal therapy.

Considering that the toxicity effects are always a concern for nanoparticles used in the field of biology, we finally examined the potential in vivo toxicity of Pd@Au-PEG. In this work, we did not notice any obvious sign of toxic side effects for Pd@Au-PEG-injected mice at the dose of 15 mg kg^{-1} within 60 d and 1 year. Neither death nor significant body weight drop was noted in the Pd@Au-PEG + laser-treated group (Figure S9a, Supporting Information). Major organs of Pd@Au-PEG-treated mice whose tumors were eliminated by the photothermal therapy were collected 60 d and even 1 year after the treatment for histology analysis. No noticeable signal of organ damage was observed from hematoxylin and eosin (H&E) stained organ slices (Figure S9b, Supporting Information), suggesting the promise of using Pd@Au-PEG for in vivo applications.

In conclusion, we have demonstrated the use of core–shell Pd@Au-PEG as a multifunctional platform as imaging contrast agents and effective hyperthermia agent for photothermal cancer therapy. Using a seeded growth method, Pd@Au nanoplates were synthesized utilizing Pd nanosheets as the seed and $AuPPh_3Cl$ as the Au precursor. When surface modified with SH-PEG, Pd@Au-PEG exhibited an excellent performance in physiological environments with a relatively long blood

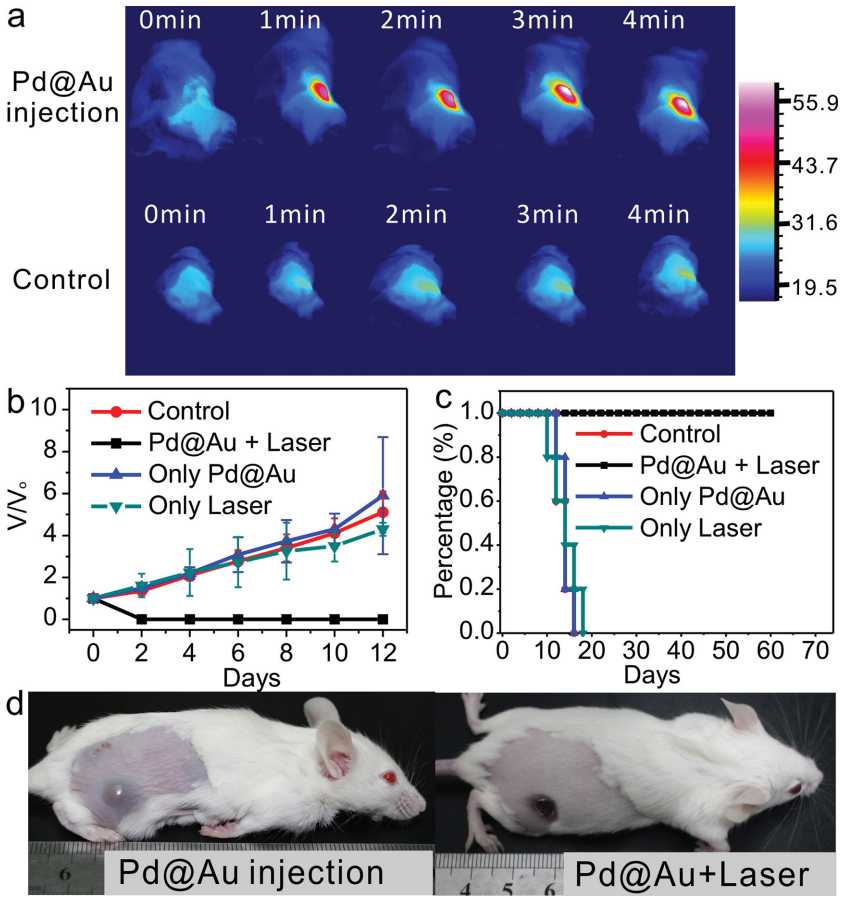

Figure 5. a) Infrared thermal images of tumor-bearing mice with and with no Pd@Au-PEG injection under 0.5 W cm^{-2} 808 nm laser. b) Relatively tumor volume of different group. Relative tumor volumes were normalized to their initial sizes. c) Survival rate curves of different groups. d) Representative photographs of mice with Pd@Au-PEG injection and photothermal cancer therapy. The tumor color was obviously blacker 24 h after Pd@Au-PEG injection, which was also an evidence for the high accumulation of Pd@Au-PEG in tumor sites.

circulation half-life time. Moreover, a surprisingly high accumulation of Pd@Au-PEG in tumor sites was achieved due to the high passive targeting by EPR effect and relatively low uptake by RES system such as the liver and spleen. The potential of Pd@Au-PEG as imaging contrast agents for both PA imaging and CT imaging was successfully demonstrated. With a high accumulation in tumor sites, photothermal cancer therapy was achieved using 808 nm laser with a power density of 0.5 W cm^{-2}, much lower than that for most reported photothermal agents. These results suggest Pd@Au-PEG as a promising theranostic agent for cancer treatment. The study provides new evidence for the superiority of 2D nanostructures for in vivo biomedical applications. Considering the presence of Pd in the core of Pd@Au nanoplates, more studies are, however, needed to evaluate their long-term safety.

Experimental Section

Reagents: $Pd(acac)_2$ (99%) was purchased from Alfa Aesar, *N*,*N*-dimethylacetamide, *N*,*N*-Dimethylpropionamide, purchased from Alfa Aesar. Tetrabutylammonium bromide, poly(vinylpyrrolidone) (PVP) (molecular weight (MW) = 30 000 g mol^{-1}) *N*,*N*-dimethylformamide, NaBr, and N_2H_4 (hydrazine) were purchased from Sinopharm Chemical Reagent Co. Ltd. (Shanghai, China). The water used in all experiments was ultrapure (18.2 MΩ). All reagents were used as received without further purification.

Synthesis of Pd Nanosheets: Pd(II) acetylacetonate ($Pd(acac)_2$, 10.0 mg), PVP (32.0 mg), and NaBr (10.2 mg) were mixed together with *N*,*N*-dimethylacetamide (2 mL) and water (4 mL) in a glass pressure vessel. The vessel was then charged with CO to 1 bar and heated from room temperature to 60 °C in 0.5 h, and then kept at 60 °C for another 2.5 h before it cooled to room temperature. Then $Pd(acac)_2$ (37.5 mg) was added to the as-synthesized seeds solution and charged with CO to 1 bar. The mixture was heated from room temperature to 60 °C in 1 h, and then kept at 60 °C for another 1 h before it cooled to room temperature. The dark blue products were precipitated by acetone, separated via centrifugation, and further purified by an ethanol–acetone mixture.

Synthesis of Pd@Au Nanoplates: For a typical synthesis of Pd@Au core–shell nanoplates, Pd nanosheets synthesized above and $AuPPh_3Cl$ (10 mg mL^{-1} in *N*,*N*-dimethylformamide) were mixed together in *N*,*N*-dimethylformamide to give a molar ratio of Au: Pd of ≈10. Then hydrazine was added dropwise while the mixture was stirred. After all the above were done, the solution was left undisturbed at room temperature for more than 12 h. The products were precipitated by acetone, separated via centrifugation, and further purified by an ethanol–acetone mixture.

Characterization: TEM studies were performed on a TECNAI F-30 high-resolution transmission electron microscope operating at 300 kV. The samples were prepared by dropping ethanol dispersion of samples onto 300-mesh carbon-coated copper grids and immediately evaporating the solvent. All the UV-Vis-NIR absorption spectra were taken on a Cary 5000 Scan UV-Vis-NIR spectrophotometer (Varian) using water as the solvent.

Xenograft Tumor Mouse Model with Tumor Cells: Female Balb/c mice (weight ≈20 g) were obtained from Shanghai SLAC laboratory Animal Co., Ltd. and all the experiments were carried out under protocols approved by Xiamen University Laboratory Animal Center. The 4T1 murine breast tumor models were generated by subcutaneous injection of 5×10^6 cells in ≈50 μL phosphate buffer solution (PBS) onto the right rear flanks of each mouse.

Photothermal Therapy In Vivo Using NIR Laser: The photothermal therapy in vivo was carried out by using an optical fiber-coupled 808 nm high power laser diode (BWT Beijing Co., Ltd.). Experimentally, the tumor on each mouse was exposed to the 808 nm NIR laser with a power density of 0.5 W cm^{-2} for 4 min. Then, the tumor sizes were measured by a caliper every other day and calculated as the volume = (tumor length) × (tumor width)^2/2. Relative tumor volumes were defined as the tumor change during the experiment, which were calculated as V/V_0 (V_0 was the initiated tumor volume when the treatment started, while V was the tumor volume during the treatment).

In Vivo NIR Imaging: To image the temperature of tumors when they were exposed to laser, an infrared thermography (HM-300, Guangzhou SAT Infrared Technology Co., Ltd.) was used to capture the temperature change on the sites of the tumors.

In Vivo PA Imaging: PA imaging was performed using Nexus 128 scanner manufactured by Endra Life Sciences (Ann Arbor, MI, USA). 700 nm were chosen as the working laser wavelength with 30 pulses

averaging. During the scanner, the water heating system maintains the water temperature at 38 °C to keep the mice comfort. PA scans were performed before the injection of the contrast agent. Then, Pd@Au nanoplates were injected into the mouse tail vein and the PA imaging was performed at different time.

In Vitro and In Vivo CT Imaging: CT imaging was acquired using Mediso nanoScan SPECT/CT produced by Mediso Ltd. Imaging parameters were as follows: slice thickness, medium; tube energy, 50 kVp, 670 μA; CTDIvol, 7279.9cGy; semicircular parameters, full scan; Number of projections, 480; In-plane voxel size, medium. All animals were scanned in the cranial to caudal direction from the lower chest to the pelvis. CT data were analyzed using the Hounsfield units (HU) for regions.

Biodistribution of Pd@Au Nanoplates: After injected with 300 μg Pd@Au nanoplates, the mice were sacrificed at 1, 12, and 24 h to obtain the major organs. At every point, there were 3–6 mice sacrificed. Then the organs were dissected and weighed for distribution studies. ICP-MS was used to measure the quantity of Au.

TEM Observation of Tumors: TEM was used to determine the location and uptake of Pd@Au nanoplates in tumor sites. Tumors of Pd@Au-injected mice were fixed in 2.5% glutar-aldehyde, 1% paraformaldehyde in 0.1 M PBS solution at 4 °C. Samples were then rinsed with PBS solution, post fixated with 1% osmium tetroxide in PBS solution at 4 °C for 1 h and rinsed with distilled water, dehydrated through a graded ethanol and acetone series, and infiltrated in Spurr's resin. Samples were then embedded in pure Spurr's resin and polymerized for 24 h at 60 °C. Ultrathin sections of ≈70–100 nm were cut with Leica UC6 and transferred to 200-mesh TEM grids. Sections were lightly stained with uranyl acetate and lead citrate and viewed on a JEOL 1400 TEM operating at 100 kV accelerating voltage.

Histology Examination: Sixty days and 1 year after the injection of Pd@Au nanoplates, major organs from the treatment group and age-matched female Balb/c control mice (without any tumor and injection of Pd@Au nanoplates) were harvested and fixed in 10% neutral buffered formalin, processed routinely into paraffin, sectioned at 10 microns, stained with H&E, and examined by a digital microscope. Tissues that were examined include the liver, kidneys, spleen, heart, and lung.

Supporting Information

Supporting Information is available from the Wiley Online Library or from the author.

Acknowledgements

This work was supported by the Ministry of Science and Technology of China (2011CB932403 and 2014CB932004) and the National Natural Science Foundation of China (21420102001, 21131005 and 81422023).

Received: September 1, 2014
Revised: September 29, 2014
Published online: October 31, 2014

[1] a) X. Zhang, Y. Xie, *Chem. Soc. Rev.* **2013**, *42*, 8187; b) Y. P. Du, Z. Y. Yin, J. X. Zhu, X. Huang, X.-J. Wu, Z. Y. Zeng, Q. Y. Yan, H. Zhang, *Nat. Commun.* **2012**, *3*, 1177; c) P. A. Hu, J. Zhang, M. Yoon, X.-F. Qiao, X. Zhang, W. Feng, P. H. Tan, W. Zheng, J. J. Liu, X. N. Wang, *Nano Res.* **2014**, *7*, 694.

[2] a) K. Yang, L. Z. Feng, X. Z. Shi, Z. Liu, *Chem. Soc. Rev.* **2013**, *42*, 530; b) K. Yang, S. Zhang, G. X. Zhang, X. M. Sun, S.-T. Lee, Z. Liu, *Nano Lett.* **2010**, *10*, 3318; c) L. Z. Feng, S. Zhang, Z. Liu, *Nanoscale* **2011**, *3*, 1252; d) L. Z. Feng, Z. Liu, *Nanomedicine* **2011**, *6*, 317.

[3] J. Li, F. Jiang, B. Yang, X. R. Song, Y. Liu, H. H. Yang, D. R. Cao, W. R. Shi, G. N. Chen, *Sci. Rep.* **2013**, *3*, 1998.

[4] a) S. S. Chou, B. Kaehr, J. Kim, B. M. Foley, M. De, P. E. Hopkins, J. Huang, C. J. Brinker, V. P. Dravid, *Angew. Chem.* **2013**, *125*, 4254; *Angew. Chem. Int. Ed. 2013, 52*, 4160; b) T. Liu, C. Wang, X. Gu, H. Gong, L. Cheng, X. Z. Shi, L. Z. Feng, B. Q. Sun, Z. Liu, *Adv. Mater.* **2014**, *26*, 3433.

[5] a) K. Yang, J. M. Wan, S. Zhang, B. Tian, Y. J. Zhang, Z. Liu, *Biomaterials* **2012**, *33*, 2206; b) L. Cheng, J. J. Liu, X. Gu, H. Gong, X. Z. Shi, T. Liu, C. Wang, X. Y. Wang, G. Liu, H. Y. Xing, *Adv. Mater.* **2014**, *26*, 1886.

[6] a) E. C. Dreaden, M. A. Mackey, X. Huang, B. Kang, M. A. El-Sayed, *Chem. Soc. Rev.* **2011**, *40*, 3391; b) G. Terentyuk, E. Panfilova, V. Khanadeev, D. Chumakov, E. Genina, A. Bashkatov, V. Tuchin, A. Bucharskaya, G. Maslyakova, N. Khlebtsov, *Nano Res.* **2014**, *7*, 325; c) N. N. Wang, Z. L. Zhao, Y. F. Lv, H. H. Fan, H. R. Bai, H. M. Meng, Y. Q. Long, T. Fu, X. B. Zhang, W. H. Tan, *Nano Res.* **2014**, *7*, 1291.

[7] R. Bardhan, S. Lal, A. Joshi, N. J. Halas, *Acc. Chem. Res.* **2011**, *44*, 936.

[8] Y. N. Xia, W. Y. Li, C. M. Cobley, J. Y. Chen, X. H. Xia, Q. Zhang, M. X. Yang, E. C. Cho, P. K. Brown, *Acc. Chem. Res.* **2011**, *44*, 914.

[9] L. M. Nie, S. J. Wang, X. Y. Wang, P. F. Rong, A. Bhirde, Y. Ma, G. Liu, P. Huang, G. M. Lu, X. Y. Chen, *Small* **2014**, *10*, 1585.

[10] a) M. P. Melancon, W. Lu, Z. Yang, R. Zhang, Z. Cheng, A. M. Elliot, J. Stafford, T. Olson, J. Z. Zhang, C. Li, *Mol. Cancer Ther.* **2008**, *7*, 1730; b) C. Loo, A. Lowery, N. J. Halas, J. West, R. Drezek, *Nano Lett.* **2005**, *5*, 709; c) J. Y. Chen, D. L. Wang, J. F. Xi, L. Au, A. Siekkinen, A. Warsen, Z.-Y. Li, H. Zhang, Y. N. Xia, X. D. Li, *Nano Lett.* **2007**, *7*, 1318.

[11] a) Z. M. Li, P. Huang, X. J. Zhang, J. Lin, S. Yang, B. Liu, F. Gao, P. Xi, Q. S. Ren, D. X. Cui, *Mol. Pharm.* **2009**, *7*, 94; b) H. N. Green, D. V. Martyshkin, C. M. Rodenburg, E. L. Rosenthal, S. B. Mirov, *J. Nanotechnol.* **2011**, *2011*, 631753.

[12] a) L. Cheng, K. Yang, Q. Chen, Z. Liu, *ACS Nano* **2012**, *6*, 5605; b) X. J. Song, H. Gong, S. N. Yin, L. Cheng, C. Wang, Z. W. Li, Y. G. Li, X. Y. Wang, G. Liu, Z. Liu, *Adv. Funct. Mater.* **2013**, *24*, 1194; c) J. T. Robinson, K. Welsher, S. M. Tabakman, S. P. Sherlock, H. Wang, R. Luong, H. Dai, *Nano Res.* **2010**, *3*, 779.

[13] W. Miao, G. Shim, S. Lee, Y. K. Oh, *Biomaterials* **2014**, *35*, 4058.

[14] X. Q. Huang, S. H. Tang, X. L. Mu, Y. Dai, G. X. Chen, Z. Y. Zhou, F. X. Ruan, Z. L. Yang, N. F. Zheng, *Nat. Nanotechnol.* **2011**, *6*, 28.

[15] a) X. Q. Huang, S. H. Tang, B. J. Liu, B. Ren, N. F. Zheng, *Adv. Mater.* **2011**, *23*, 3420; b) M. Chen, B. H. Wu, J. Yang, N. F. Zheng, *Adv. Mater.* **2012**, *24*, 862.

[16] X. Fan, Z. R. Guo, J. M. Hong, Y. Zhang, J. N. Zhang, N. Gu, *Nanotechnology* **2010**, *21*, 105602.

[17] a) P. Huang, J. Lin, W. W. Li, P. F. Rong, Z. Wang, S. J. Wang, X. P. Wang, X. L. Sun, M. Aronova, G. Niu, R. D. Leapman, Z. H. Nie, X. Y. Chen, *Angew. Chem.* **2013**, *125*, 14208; *Angew. Chem. Int. Ed. 2013,52*, 13958; b) P. Huang, P. F. Rong, J. Lin, W. W. Li, X. F. Yan, M. G. Zhang, L. M. Nie, G. Niu, J. Lu, W. Wang, *J. Am. Chem. Soc.* **2014**, *136*, 8307; c) Q. W. Tian, F. R. Jiang, R. J. Zou, Q. Liu, Z. G. Chen, M. F. Zhu, S. P. Yang, J. L. Wang, J. H. Wang, J. Q. Hu, *ACS Nano* **2011**, *5*, 9761; d) C. M. Hessel, V. P. Pattani, M. Rasch, M. G. Panthani, B. Koo, J. W. Tunnell, B. A. Korgel, *Nano Lett.* **2011**, *11*, 2560.

[18] X. W. Liu, H. Q. Tao, K. Yang, S. Zhang, S.-T. Lee, Z. Liu, *Biomaterials* **2011**, *32*, 144.

[19] C. B. Gao, J. Vuong, Q. Zhang, Y. D. Liu, Y. D. Yin, *Nanoscale* **2012**, *4*, 2875.

[20] C. Kim, C. Favazza, L. H. V. Wang, *Chem. Rev.* **2010**, *110*, 2756.

[21] a) Z. B. Zha, Z. J. Deng, Y. Y. Li, C. H. Li, J. R. Wang, S. M. Wang, E. Z. Qu, Z. F. Dai, *Nanoscale* **2013**, *5*, 4462; b) G. Ku, M. Zhou,

S. L. Song, Q. Huang, J. Hazle, C. Li, *ACS Nano* **2012**, *6*, 7489; c) J. V. Jokerst, A. J. Cole, D. Van de Sompel, S. S. Gambhir, *ACS Nano* **2012**, *6*, 10366.
[22] Y. Liu, K. Ai, L. Lu, *Acc. Chem. Res.* **2012**, *45*, 1817.
[23] a) P. Huang, L. Bao, C. L. Zhang, J. Lin, T. Luo, D. P. Yang, M. He, Z. M. Li, G. Gao, B. Gao, *Biomaterials* **2011**, *32*, 9796; b) C. Peng, L. F. Zheng, Q. Chen, M. W. Shen, R. Guo, H. Wang, X. Y. Cao, G. X. Zhang, X. Y. Shi, *Biomaterials* **2012**, *33*, 1107; c) R. Popovtzer, A. Agrawal, N. A. Kotov, A. Popovtzer, J. Balter, T. E. Carey, R. Kopelman, *Nano Lett.* **2008**, *8*, 4593; d) D. Kim, S. Park, J. H. Lee, Y. Y. Jeong, S. Jon, *J. Am. Chem. Soc.* **2007**, *129*, 7661.